Effect of exposure time on corrosion behavior of zinc-alloy in simulated body fluid solution: Electrochemical and surface investigation

Deepti Jain, Shubhra Pareek, Arunava Agarwala, Rahul Shrivastava, Wafa Sassi, Saroj Parida, Debasis Behera

Available online at www.sciencedirect.com

jmr&t Journal of Materials Research and Technology

journal homepage: www.elsevier.com/locate/jmrt

Original Article

Effect of exposure time on corrosion behavior of zinc-alloy in simulated body fluid solution: Electrochemical and surface investigation

Deepti Jain [a,1], *Shubhra Pareek* [a], *Arunava Agarwala* [a], *Rahul Shrivastava* [a], *Wafa Sassi* [b,c], *Saroj K. Parida* [d], *Debasis Behera* [e,1,*]

[a] *Department of Chemistry, School of Basic Sciences, Manipal University Jaipur, Jaipur, Rajasthan, 30300, India*
[b] *Équipe Sonochimie et Réactivité des Surfaces (SRS), Institut UTINAM, Université de Franche-Cometé, Besançon, France*
[c] *UREME (UR17ES45), Faculté des Sciences de Gabés, UNiversité de Gabès, Cité Erriadh, 6072, Gabès, Tunisia*
[d] *Department of Physics, National Institute of Technology Agartala, Tripura, 799046, India*
[e] *School of Chemistry, Gangadhar Meher University, Amruta Vihar, Sambalpur, Odisha, 768004, India*

ARTICLE INFO

Article history:
Received 25 September 2020
Accepted 16 December 2020
Available online 24 December 2020

Keywords:
Zinc alloy
Simulated body fluid
Biocompatibility
Electrochemical measurements
Scanning electron microscopy
X-RAY Photoelectron spectroscopy

ABSTRACT

Zn alloy biocompatible implant materials have wide clinical application but its susceptibility to corrosion in the physiological environment due to increased exposure time is a major constraint. Consequently, diverse electrochemical responses have been investigated to understand the corrosion mechanism at the Zn alloy interface in different immersion times up to 168 h. A self-protective layer of $Zn(OH)_2$ was evidenced over the surface of Zn alloy at higher exposure time in simulated body fluid (SBF) solution. The morphology and chemical composition of the zinc surface has been studied by Field emission scanning electron microscopy (FESEM), X-RAY diffraction (XRD), annulated transmission refraction (ATR), and X-RAY Photoelectron Spectroscopy (XPS). The results indicated that the Zn alloy predominantly forms zinc oxide or hydroxide and zinc phosphate compound as primary corrosion products at the interface which is confirmed from the elemental ratio (Zn/O, Zn/Cl and Zn/P 1:1, 1:2, 2:3 respectively). Additionally, FESEM results confirmed the selective formation of nano structured $Zn(OH)_2$ which is responsible for the protectiveness of zinc specimen at higher exposure period. When Zn alloy was immersed in SBF solution, the corrosion rate was found to be 0.156–0.0976 mmy^{-1}, which proves the sustainability of Zn alloy for biomedical applications and provides an improved degradation mechanism of Zn alloy in SBF solution.

* Corresponding author.
E-mail address: dbahera@gmail.com (D. Behera).
[1] Both authors contributed equally to this work.
https://doi.org/10.1016/j.jmrt.2020.12.050

1. Introduction

Bioabsorbable materials are widely used in biomedical application [1]. A few common metallic materials like Stainless steel [2], titanium and its alloy [3,4], cobalt based alloy are also used as bioabsorbable material [5,6]. Sometimes these materials are required to be removed by second surgery. An ideal orthopedic implant should have mechanical as well as biodegradable properties. It is also assumed that during the process of degradation, the final product should be non-toxic to the human body and slowly degrade and get absorbed inside the body.

Since the last few years, Mg and Fe have been used in orthopedic implantation. During the degradation process Mg and its alloy show a high corrosion rate and release hydrogen gas. Fe and its alloy also have a slow degradation rate and form an oxide layer which repels the neighboring cells. Ghoneim et al. investigated the corrosion performance of the AZ91E magnesium alloy that was used as a staple in Sleeve Gastrectomy surgery. They investigated that potassium sorbate is used as an inhibitor for antimicrobial and food preservative substances [7]. R. S. El-Kamel investigated that the Graphene oxide nanoparticles/polythreonine polymer nano-coating on AZ91E Mg alloy is used new implant material for Gastrectomy application [8]. Fekry et al. investigated electrochemical corrosion behavior of a novel nano-composite coating on Ti alloy in phosphate buffer solution. They examined the novel nano-coating which shows highly antimicrobial activity as compared to bare metal [9]. A silver nanoparticle/graphene oxide/chitosan nano-composite coating is used for food safety. These nanocomposites show high protection efficiency (99.0%), which is verified by polarization curve [10]. Farghali et al. investigated a highly uniformed nano-composite film of chitosan and gold nanoparticle on Ti alloy. They studied that Ti alloy shows higher impedance value and phase angle for AuNps/CS biocomposite for Nyquist and Bode plot [11]. Ameer et al. investigated electrochemical and interface analysis of Ti alloy in SBF solution. They investigated that the Ti alloy forms a protective layer on the surface, in addition to 0.95% by weight raftiline inulin in the presence of 10^{-5} M calcium levulinate [12]. Chitosan biocomposite coating was reinforced with the multiwalled-carbon nanotubes and it increases the stability, corrosion resistance and bioactivity of the Ti −6Al−4V alloy and the calcium carbonate ($CaCO_3$) was used for the surface modification by electroless deposition [13]. Moreover, Zinc and its alloys are also used in biomedical application due to its biodegradable nature and ideal dissolution rate [14–16]. Zinc is an essential component of many enzymes and also involved in various metabolic activities [17]. 15 mg/day Zinc is recommended in the daily diet by dieticians [18]. Zinc has many important biological functions like gene expression [19], food ingestion and growth [20] wound healing [21], cell division [22], DNA replication or regeneration [23] and acts as enzymatic co-factor in many reactions [23–26]. In many metabolic activities, zinc helps in absorption of ions and amino acid complexes through the small intestine and regulates them with the help of organs like pancreas, liver, kidney [27–29].

Metallic zinc has various properties similar to human bones like tensile strength (126–246 MPa), Young's modulus (70 GPa) and density (7.14 g/cm$^{3)}$. Zinc alloy has high mechanical properties and a low melting point to convert easily into casting materials. Zinc alloy is non-toxic to the human body. Zn-1X binary alloy shows low corrosion rate *in vivo* and *in vitro* conditions [30]. Zn -1Li shows good cytocompatibility *in vivo* condition before and after 1–3 months [31]. Zn–Al alloy demonstrates stable corrosion rates after 2 years *in vivo* condition [32]. In Zn–Mg alloy, the addition of Mn, increases the susceptibility of micro galvanic corrosion and improves the casting process [33]. Zn–Mg alloy increases the mechanical properties of the material [34]. Addition of Cu alloy with Zn, increases its ductility and elongation nature at different amounts of concentration [35–37].

Metallic zinc has been used in rabbit's vascular stents due to the slow dissolution rate, high tensile strength and ductility [38]. Various studies have also taken place on this subject matter like Bowne et al. has used zinc stents in abdominal aorta of rats due to its bioabsorbable nature, biocompatibility and ability to reduce the inflammation that occur due to degradation products [16]. Same as Li et al. also found that Zn–1Mg alloy in mouse femora doesn't have any negative effect on its health and also formed a strong new bone [30]. This indicates that Zn alloy can also be used *in vivo* conditions as a bioabsorbable stent in orthopedic implantation. Torne et al. found that the corrosion rate of Zn alloy is increased when it is exposed in the simulated phosphate buffer saline (PBS), Ringer solution and decreased when present in physiological body fluids. It is due to passivation film in simulated fluid which has a thick layer of corrosion products [39].

Zn^{+2} ion is also found in human bone marrow mesenchymal stem cells (hMSC) and human vascular cells ((HCECs, HASMC, HAEC) [40–43]. Zhu et al. has also found that cell proliferation and hMSC cell adhesion is supported by the zinc metal and Zn^{+2} ions regulate gene expression and cell growth [42]. Human plasma, Ringer solution, Henk's solution, phosphate buffer saline (PBS) and different types of simulated body fluids are used as artificial mimicking solutions for orthopedic implantation because these solutions contain similar composition as blood plasma [39,44–50].

From the thermodynamic point of view, standard electrode potential of Zn lies between Mg and Fe, i.e. Mg (−2.37 V) < Zn (−0.763 V) < Fe (−0.440 V). From this, it can also be predicted that Zn can fulfill clinical demand as it has a middle degradation rate.

In this research paper, the primary corrosion behavior of Zn alloy in a simulated body fluid is examined. The corrosion rates of Zn alloy in SBF at different immersion times are observed by electrochemical measurement and immersion tests. Interfacial processes like charge transfer, diffusion and absorption of species are studied by EIS. Finally, the corrosion mechanism which is given in this study explains about the degradation process of Zn alloy and its product formation. This study can be beneficial for in-vitro studies to choose the suitable solution for biomedical zinc alloy.

Table 1 – Elemental composition Zn alloy by OES technique.

Element	Pb	Al	Cu	Ce	Mn	La	Mg	Fe	Si	Zn
Wt/Wt%	0.002	0.010	0.021	0.046	0.047	0.073	0.951	1.12	1.23	96.5

2. Materials and method

2.1. Sample preparation

Commercially available zinc alloy (96.5% Zn) was used for the chemical, electrochemical and morphological surface experiments and the alloy composition is given in Table 1 which is obtained by optical emission spectroscopy (OES) from MRC lab MNIT Jaipur. The specimens were cut into 3 mm × 2 mm × 0.3 mm dimensions for the immersion test and 1 cm^2 area was used for electrochemical measurements. Samples were grounded with silicon carbide emery papers up to 2000 grade and then ultrasonically cleaned with ethanol and acetone, dried in the air. The specimens were then etched 5–10 s in Kroll's reagent (H_2O: HF: HNO_3 = 1.5:2.5:6) to remove native oxide layer from the surface.

2.2. Physiological solution preparation

SBF solution simulates the physiological environment similar to human blood plasma [38] for investigation of Zn alloy corrosion (see ESI†, Table 1). It was prepared by mixing different concentrations of inorganic compounds as per the reported approach [51].

2.3. Electrochemical measurement

The electrochemical measurements were performed by using a Computer controlled Electrochemical Workstation (Potentiostat, Biological Science instrument, SP-150, FRANCE) with one compartment three electrode setup viz. Zn alloy with an exposed area of 1 cm^2 as working electrode, platinum mesh as counter electrode, and Ag/AgCl as working reference electrode. The experiments were performed in 250 mL of SBF solution by immersing the specimens for 2 h to establish the stable open circuit potential (OCP). The range of frequency was between 100 kHz and 10 mHz at open circuit potential with 10 mV sinusoidal amplitude and 10 points per decade were employed for each impedance data measurements. Appropriate equivalent circuits were chosen based on fitting data to elucidate interfacial electrochemical mechanisms of Zn specimens. After impedance measurements, potentiodynamic polarization studies were done at a scan rate of 1 mV/s and scan range from cathodic to anodic direction in a potential window of −3.25 to −0.25 V.

2.4. Immersion test

Corrosion behavior of Zn alloy in SBF solution was studied using the immersion test. The Zn alloy was immersed in 250 mL solution with an exposed total surface area of 1 cm^2, pH 7.2–7.6 adjusted by 1 M HCl. pH values of the solution were recorded before and after the immersion of specimens for different exposure periods. The corrosion behavior and formation of corrosion products were examined up to 168 h immersion time. The formed corrosion products during immersion test were removed by cleaning the specimen in a solution containing 200 g/L to obtain exact weight loss [52]. The samples were cleaned with distilled water and rinsed with acetone and were dried before weighing. In addition, the corrosion rate was calculated by the following equation [53].

$$CR = 87.6 \times \Delta W \div A \times T \times D \quad (1)$$

Where.

CR = Corrosion rate, mmy^{-1}

ΔW = Total weight loss of sample, mg.

A = Original surface area exposed to the test solution, cm^2

T = Exposure time, hour.

D = Density of metal, g/cm^3

2.5. Surface morphology and component analysis

The cleaned and oxide free specimens were immersed in 250 mL of SBF solutions for different immersion periods. Specimen's morphology was analyzed by Field Emission scanning electron microscope instrument (FE-SEM, Nova nano 450 (FEI), Netherland) at room temperature. Besides, energy dispersive X-ray spectrometer (EDS) was used for elemental compositions. Attenuated total reflectance Fourier transform infrared spectroscopy (ATR-FTIR, Alpha, Bruker, Germany) technique was used to discover the functional groups in corrosion products on the sample surface an immersion period up to 168 h in the 4000-600 cm^{-1} wavenumber range. X-ray diffraction pattern (XRD, Panalytical X Pert Pro, UK) was applied to identify the phase composition of the samples. The surface chemical composition and chemical state of the specimens was measured after exposure in SBF solution at a different immersion time by X-ray photoelectron spectroscopy (XPS, Oxford instrument, Omicron ESCA, Germany). XPS spectra were recorded using Al Kα monochromatized X-ray radiation and the energy of excitation was 1486.6 eV with a resolution of 0.60 eV. The surface topographies (2D and 3D) were performed quantitatively through tapping mode of atomic force microscope (AFM, Bruker, MRC Jaipur).

3. Results and discussion

3.1. Electrochemical analysis

3.1.1. Open circuit potential (OCP)

OCP *vs* time values were obtained under a non-polarized condition after 2 h immersion of Zn specimens in the test solution shown in Fig. 1. The potential value changes in the positive direction over the time due to the dissolution of the bare metal surface in the SBF solution and complete removal

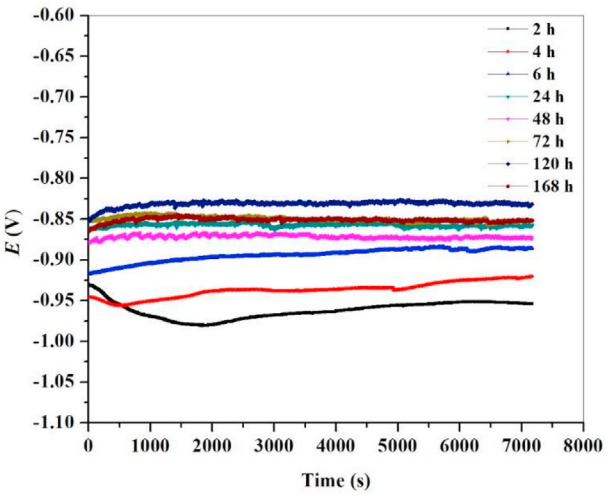

Fig. 1 – Open Circuit Potential of Zn alloy in SBF solution at a different immersion time.

of pre-formed ZnO film on the Zn alloy surface [54–60]. After 2 h of the metal immersion, the oxide film formation occurs in the presence of inorganic ions. However, the time taken in the formation of the oxide/hydroxide layer was much less and depends upon the concentration of other anions. Invariably alter the behavior, this less time may be attributed to the dissolution of the metal. The presence of the inorganic anions concentration, depends on the formation of a corrosion product and causes the potential of zinc electrode. The open circuit potential (OCP), starts to shift into the noble direction to reach steady values which becomes more positive (anodic) as the immersion time is increased [59,61].

It is clear from Fig. 1 that all OCP values are for 4 h (−0.945 V), 6 h (−0.865 V), 24 h (−0.858 V), 48 h (−0.857 V), 72 h (−0.853 V), 120 h (−0.832 V), 168 h (−0.852 V) respectively and more than 2 h (−0.953 V *vs.* Ag/AgCl) and are shifted in anodic direction with respect to time. It had also been seen that the value of OCP for 168 h decreased and has shifted to the cathodic direction. The reverse trend may be responsible for the breakdown of the corrosion product on the surface. The variation in OCP for various immersion periods, indicates a continuous change in the morphology of metal surfaces and corrosion products.

3.1.2. *Electrochemical impedance spectroscopy (EIS)*

Nyquist plot for Zn alloy in SBF solution for various periods of immersion (Fig. 2) reveals two depressed capacitive semicircles between 4 h and 48 h, which gives a clear existence of two different interfaces between Zn alloy and SBF solutions. The small capacitive semicircles appearing in the high frequency region and the large capacitive semicircles corresponding to the low frequency region are attributed to the charge transfer and surface film formation respectively at the interface in SBF solution. But the absence of first depressed capacitive semicircle in Fig. 2 (a) gives an evidence of non-existence of film formation. Whereas, capacitive loop is observed in all cases with increasing exposure period from 4 to 168 h. Inductive loop is absent in the low-frequency region which indicates the absence of the flow of electrolyte on the metal/film surface. Capacity growth increases the diameter of the high-frequency capacitive semicircle. The diameter of the high frequency capacitive loop increases with immersion time resulting in high impedance values, this is due to the existence of the passive film. In addition, the film impedes the entry of aggressive ions on the surface of the metal, thereby decreasing the kinetics of the corrosion process [62]. It is also assumed that the Fe present in Zn alloy in the form of precipitate to form a stable passive layer and indicates absorption of corrosive ions [63,64]. However, disappearance and deviation in first capacitive semicircles have been observed beyond 72 h of exposure period. Only one capacitive semicircle has appeared and the low-frequency region shows the deviation which may be due to the sample polarization.

EIS models were fitted to appropriate equivalent circuit models and data are listed in Table 2. Analysis of Table 2 reveals that the high values of solution resistance, R_1 are observed for longer exposure period (123.8 Ω and 128.0 (Ω) for 120 h and 168 h respectively), which is consistent with the fact that degradation of passive film occurs due to bulk of SBF solution resulting reduction of first capacitive semicircles. Here, R_1 is the solution's resistance and Q_1 is the constant phase element for anodic film formation, which is exhausted in the place of capacitor to compensate for the non-homogeneity and roughness of the system and used as the double layer capacitance (C_{dl}). The double layer capacitance and the CPE value of a film can be evaluated by following equations [65].

$$Z_{CPE} = \frac{1}{Y_{\circ}(j\omega)^{\alpha}} \tag{2}$$

$$C_{dl} = Y_{\circ} \times (\omega_{max})^{(\alpha-1)} \tag{3}$$

where, Z is the impedance of polarized electrode, which contains a capacitance (CPE), ω is the angular frequency of the input signal. Y_0 represents the proportional factor and $j = \sqrt{-1}$ is the imaginary root. Where $\alpha = 1$ represents the pure capacitance of the surface or $\alpha \neq 1$ the system shows the surface roughness.

$$C_{dl} = \frac{\varepsilon_{\circ}\varepsilon A}{d} \tag{4}$$

where, d is the thickness of the film, A is the exposed surface of the electrode in SBF solution, ϵ_0 is the permittivity of the vacuum, ϵ is the local dielectric constant. C_{dl} value increases due to the formation of nano-strands and nano-fibers $Zn(OH)_2$ corrosion product on the surface of the alloy. The corrosion product is dissolved in the solution and formed on the alloy surface, respectively. As a result the dielectric constant (ϵ) of the solution with increasing double layer thickness.

The anodic electrochemical reaction comprises the charge transfer resistance between the metal surface and interface (R_2) in parallel with the double layer capacitance [66]. R_3 is the resistance of film formation and parallel to the C_3. C_1 is the double layer capacitance due to the charge transfer between the interface and the metal alloy. C_3 is the capacitance of $Zn(OH)_2$ corrosion product layer. This indicates the formation of a passivation film on the metal surface. Value of R_2 and R_3 is

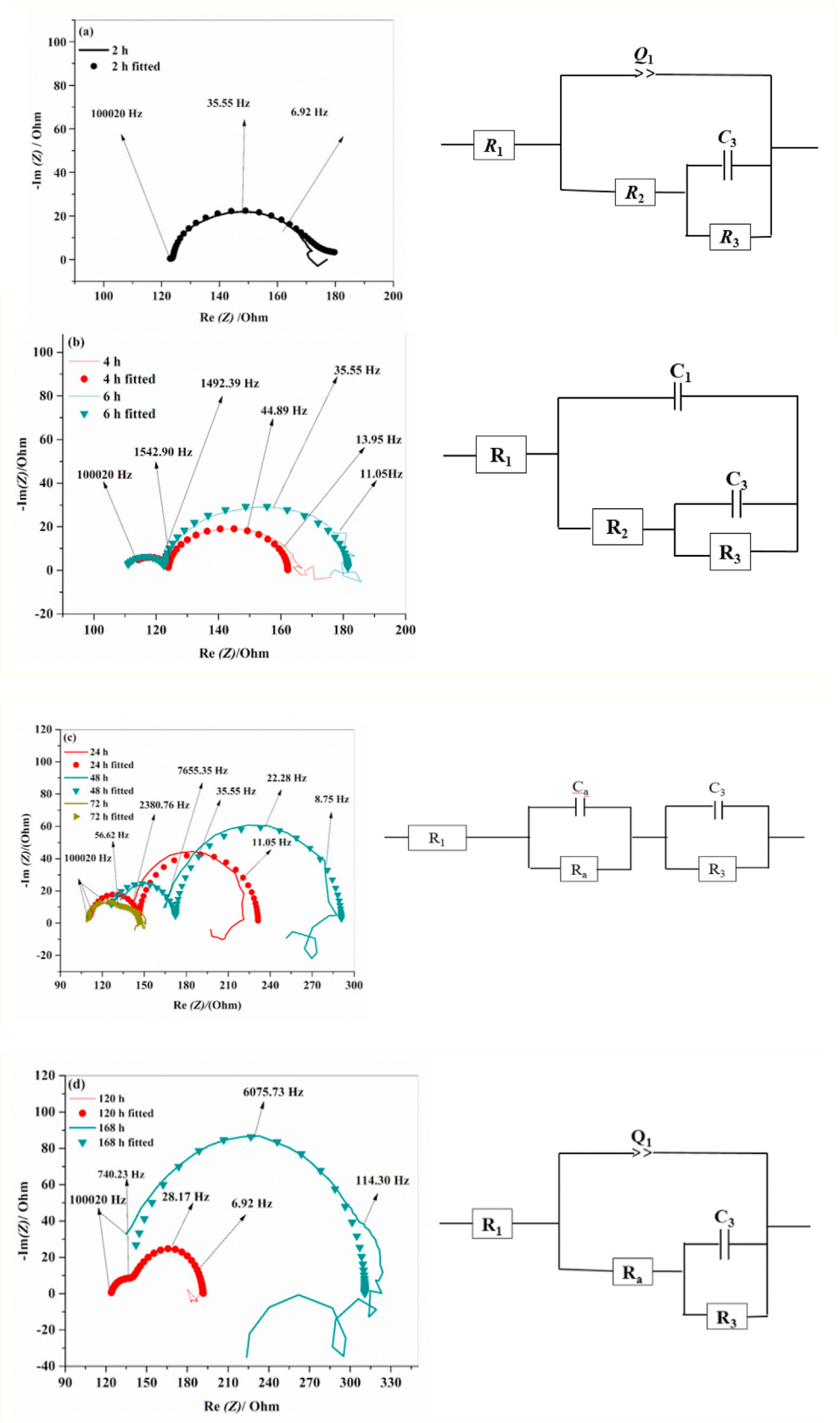

Fig. 2 – Nyquist plot (Left) corresponding equivalent circuit (Right) after immersion time (a) 2 h (b) 4 h and 6 h (c) 24 h and 48 h (d) 120 h and 168 h.

Table 2 – EIS fitting data after various immersion times in SBF solution.

Immersion time (h)	R_1 ($\Omega.cm^2$)	Y_0 ($\times 10^{-3}Scm^2S^{(\alpha-1)}$)	α_1	C_{dl} ($mF.cm^{-2}$)	C_1 ($\mu F.\ cm^{-2}$)	C_2 ($\mu F.\ cm^{-2}$)	R_2 ($\Omega.\ cm^2$)	C_3 ($\mu F.\ cm^{-2}$)	R_3 ($\Omega.\ cm^2$)	R_p ($\Omega.cm^2$)
2	109.7	3.69	0.103	149.94	–	–	16.69	67.16	79.85	96.51
4	119.7	–	–	–	0.260	–	12.07	83.15	38.22	50.29
6	110.3	–	–	–	0.543	–	12.51	67.18	58.66	71.17
24	110.9	–	–	–	–	0.3146	35.28	64.12	85.12	120.4
48	123.5	–	–	–	–	0.1292	48.82	58.80	118.12	167.4
72	109.5	–	–	–	–	0.6782	23.45	10.53	13.44	36.89
120	123.8	44.2	0.791	21997.0	–	–	22.12	86.4	45.75	67.87
168	128.0	20.9	0.809	80860.0	–	–	10	93.5	180	190

increased with immersion time for 24 h and 48 h and the value of R_2 and R_1 is decreased for 72 h. This is a direct indication for the formation of a passive film on the metal surface and the tendency for C_2 and C_3 to decrease in the same potential area also contributes to the formation of a passive film. When the immersion time is increased, it results in the high frequency capacitive loop disappearance due to breakdown of passive film layer. After increasing the exposure time, the value R_1 and R_2 is decreased for 120 h and increased for 168 h. This shows the equilibrium phase between the metal alloy and solution. After increasing the time, the value is also increased which is the direct evidence of formation of a corrosion product layer on the metal alloy surface. Polarization resistance increases from 2 h to 48 h and decreases after 72 h–120 h. This process is showing the formation of a protective on the Zn alloy surface.

3.1.3. *Potentiodynamic polarization test*

Fig. 3 shows the potentiodynamic polarization (PDP) curves for Zn alloy in SBF solution up to 168 h. The passive layer and dissolution area formation take place on anodic region. In the cathode area, hydrogen evolution is the possible electrochemical reaction. In most corrosion experiments, the anodic area is most crucial as compared to the cathodic area, as the metal surface passes through various oxidative changes, which begins in a dissolution of metal specimen. Therefore, the anodic area is more helpful to elucidate the corrosion potential of Zn alloy in the SBF solution. In the SBF solution, the corrosion potential of Zn alloy is approximately 1.20 V, where both anodic and cathodic reactions are in equilibrium as shown in Fig. 3. As a result, it is clear that the anodic area is attributed to the passive film on the Zn alloy surface in the SBF solution. Corrosion potential (E_{corr}), corrosion current density (i_{corr}), Anodic Tafel slope (β_a), Cathodic Tafel slope (β_c) are related parameters of the PDP curve shown in Table 3. It is clearly seen that the values of corrosion potential (E_{corr}) are increasing with increase in exposure time and form corrosion products in the anodic region. Zn alloy forms a thin hydroxide layer in anodic area, which is responsible for the dissolution of the bare metal. The corrosion potential is shifted in a negative direction with exposure time. The corrosion current density (i_{corr}) is also increased with exposure time, which is responsible for the breakdown of the metal alloy and formation of corrosion product on the metal surface, while the i_{corr} results are found, decreasing at 120 h and 168 h due to intrinsic stable protective layers of corrosion products, which corroborate the

Table 3 – Summary of potentiodynamic polarization at a different immersion time in SBF.

Time (h)	$-E_{corr}$ (mV/Ag/AgCl)	i_{corr} ($\mu A/cm^2$)	β_a (mV/dec)	β_c (mV/dec)	R_p ($\mu\Omega.cm^2$)
2	1197.997	29.995	0.002	0.001	0.0781
4	1319.576	20.837	0.001	0.010	0.995
6	1250.683	25.413	0.002	0.010	2.64
24	1314.869	38.741	0.001	0.010	18.4
48	1213.356	52.250	0.004	0.010	13.6
72	1311.810	74.431	0.002	0.009	63.9
120	1329.771	54.560	0.003	0.011	99.5
168	1387.355	57.285	0.002	0.010	64.5

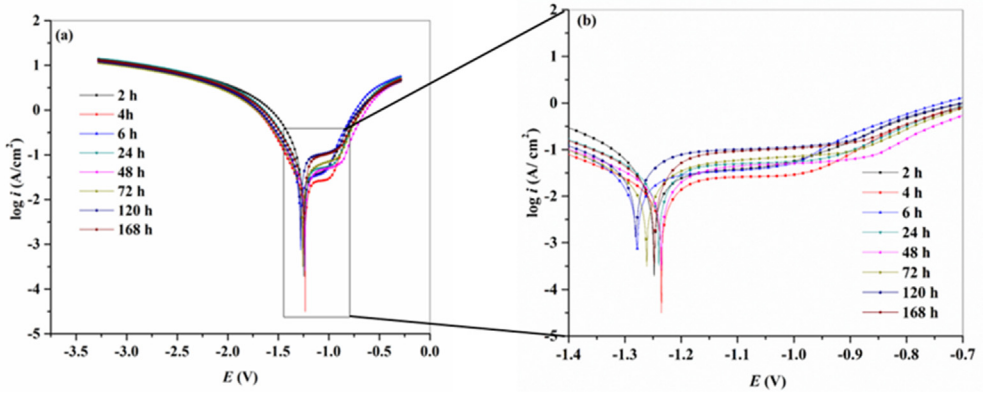

Fig. 3 – (a) The Potentiodynamic polarization curve of Zn alloy at a different immersion time period in SBF solution (b) magnified polarization curve for the selected area.

Table 4 – Corrosion rates of Zn alloy in the SBF solution at various immersion times (CR_w, mmy^{-1}).

Immersion Time (h)	Weight loss (mg/cm^2)	Corrosion rate (mmy^{-1})
2	0.25	0.1569
4	0.41	0.1261
6	0.75	0.1550
24	1.14	0.0583
48	1.89	0.0482
72	2.32	0.0397
120	2.83	0.0289
168	2.97	0.0147

findings of Impedance results. The potentiodynamic polarization is measured by the Stern Geary equation [67]. Here, R_p is the polarization Resistance (see Table 3).

$$R_p = \frac{\beta_a \times \beta_c}{2.303 \times i_{corr}(\beta a + \beta_c)} \quad (5)$$

3.2. *Proposed dissolution mechanism of Zn alloy in SBF*

When zinc alloy is immersed in SBF solution, Zn metal is oxidized to Zn^{+2} and H_2 is produced by a reduction of water in accordance with the following reaction (Fig. 4)

$$Zn \rightarrow Zn^{+2} + 2e^- \quad (6)$$

$$H_2O + 2e^- \rightarrow OH^- + H_2 \quad (7)$$

Zn^{+2} reacts with OH^- ion to form metal hydroxide near the metal surface and dehydration of $Zn(OH)_2$ occurs to from ZnO [68,69] in Fig. 4 (a)

$$Zn^{+2} + 2OH^- \rightarrow Zn(OH)_2 \quad (8)$$

$$Zn(OH)_2 \rightarrow ZnO + H_2O \quad (9)$$

When the immersion time is extended to 168 h the maturing and thickening of the accumulating $Zn(OH)_2$ layer of the sample. The $Zn(OH)_2$ forms a layer of precipitate on the specimen surface. The sample is contributing to the degradation of Zn alloy. The whole surface of Zn alloy was nearly converted to corrosion product. The formation of zinc oxide contributes to the nucleation of carbonate compounds. $ZnCO_3$ with a constant solubility precipitates product mainly due to a large amount of liberated Zn^{+2} ions near the surface in Fig. 4 (b).

$$HCO_3^- + OH^- \rightarrow CO_3^{-2} + H_2O \quad (10)$$

$$Zn^{+2} + CO_3^{-2} \rightarrow ZnCO_3 \quad (11)$$

The carbonate particles continue to grow with long immersion time. As a result, the sample surfaces get covered with corrosion products. However, the weight loss continuously is increased with immersion time summerized in Table 4. At this time, the Zn and Ca^{+2} react with PO_4^{-3} and is turned into a compound Zn $(PO_4)_3$ or Ca_3 $(PO_4)_2$ as the following reaction in Fig. 4 (c).

$$HPO_4^{-2} + OH^- \rightarrow PO_4^{-3} + H_2O \quad (12)$$

$$Zn^{+2} + PO_4^{-3} \rightarrow Zn_3(PO_4)_2 \quad (13)$$

$$Ca^{+2} + PO_4^{-3} \rightarrow Ca_3(PO_4)_2 \quad (14)$$

Partial dissolution of corrosion products cannot protect the Zn substrate effectively, as it is leading to the increase in i_{corr} with the immersion time after 168 h and a stable corrosion product formed on the metal surface.

3.3. *Immersion test*

3.3.1. *pH assessment, dissolution and weight loss studies*

Fig. 5 Shows changes in pH *vs* time for the Zn alloy samples immersed in 250 mL of simulated body fluid. The pH is increased with increase in time, which may be ascribable to the formation of Zn $(OH)_2$ in the solution. The pH assessments of SBF as a component of immersion time are presented in Fig. 5 (a) which shows a linear increase in pH of the SBF arrangement. It was found at the basic immersion up to 72 h. This is due to the formation of increasing OH^- ions in the solution. Thereafter, a low increment in pH was seen by further immersion from 120 h to 168 h and after that a moderately steady pH of 7.97 was observed. As can be seen in Fig. 5 (b), the dissolution rate of Zn^{2+} was quick in the 72 h immersion and turned out to be moderate amid further

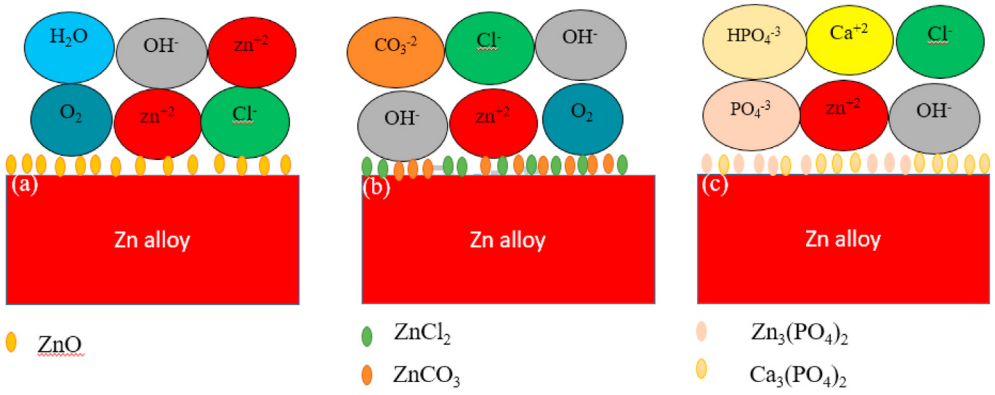

Fig. 4 – Schematic diagram of proposed mechanism of corrosion process of Zn alloy immersed SBF solution (a) formation of ZnO (b) formation of $ZnCl_2$ and $ZnCO_3$ (c) formation of $Zn_3(PO)_4$ and $Ca_3(PO)_4$.

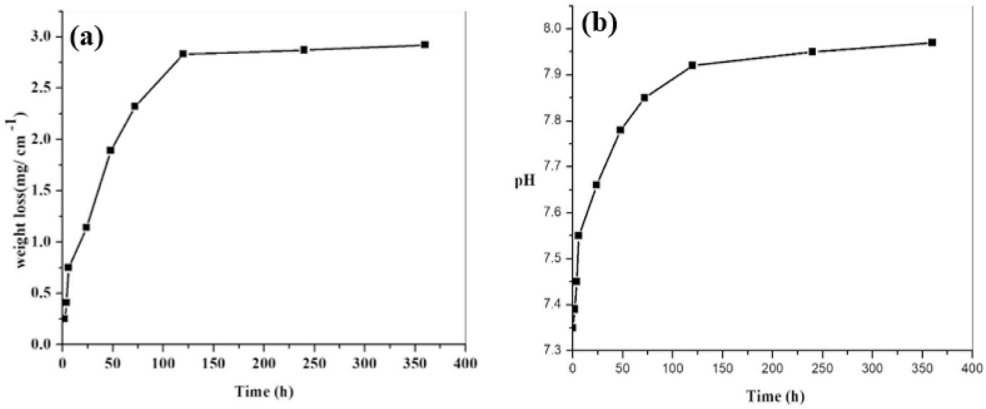

Fig. 5 – Variation in (a) weight loss of Zn alloy in the SBF solution (b) pH Values as a function of the immersion time.

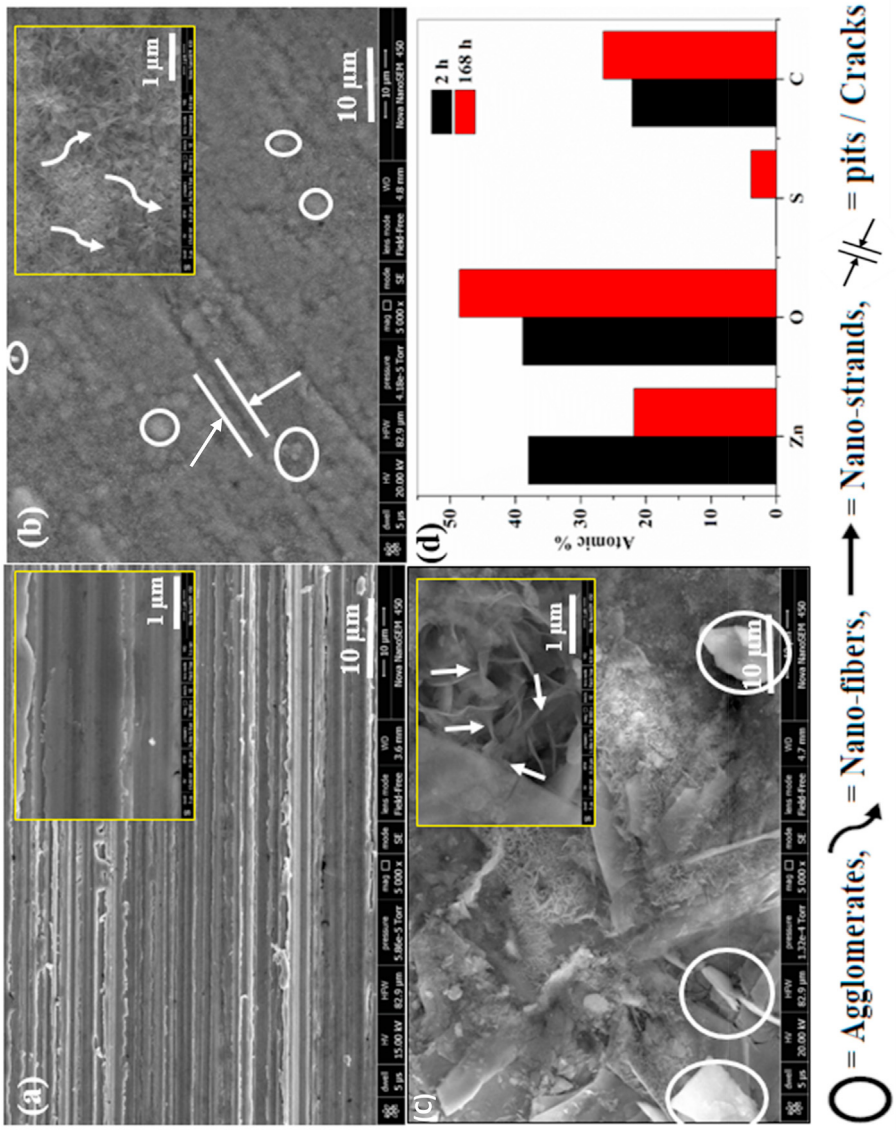

Fig. 6 – FESEM I mages of Zn alloy immersed in SBF solution for (a) Polished, (b) 2 h, (c) 168 h (The insets show the magnified FESEM images in the squared area) and (d) atomic % obtained from EDX spectra.

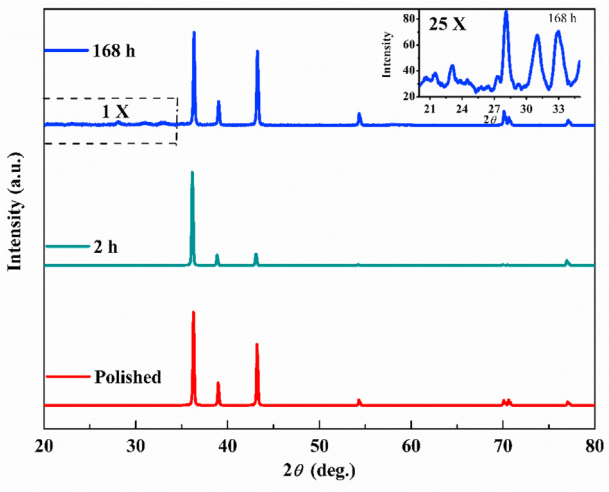

Fig. 7 – XRD spectra of Zn alloy in SBF solution for different immersion time.

immersion. After 120 h, the accumulated Zn^{2+} discharge was around 2.83 mg cm^{-2}. The weight loss of Zn alloy (see Table 4) expanded insistently with 168 h time and achieved 2.97 mg cm^{-2} to the continued dissolution of Zn alloy in the SBF. The formed oxide layer may exhibit rectifying characteristics similar to their anodically formed passive films layer [55,70]. It is assumed that the thickness of the oxide film layer is increased with immersion time. This thickness of the passive film layer is controlled by the immersion time and corrosivity of the surrounding environment [43]. In the solution, presence of some aggressive ions is incorporated with the ZnO surface and substitutes some oxide ions in the oxide layer film. In the solution, the presence of aggressive ions like Cl^{-},PO_4^{-3}, HPO_4^{-2}, SO_4^{-2} is incorporated in the ZnO/$Zn(OH)_2$ film and affect its properties [71,72]. According to a complex ion theory of corrosion, aggressive anions may substitute some oxide ion in the oxide film and form chemical species in the medium. Dissolution of the metal depends upon the relative stability of ions and the nature of anions [70,73].

3.4. *Surface analysis*

3.4.1. *FESEM analysis*

Fig. 6 (a) and (b) show the micrographs of the Zn alloy specimens before and after immersion in SBF solution. Fig. 6 (a) depicts the smooth polished surface of Zn alloy and some scratches marks during abrasion. However, Fig. 6 (b) illustrates the corroded rough surface due to the aggressive attack from the corrosive solution. The formation of some short fibers is witnessed in 6 (b) due to the formation of zinc hydroxide on metal specimens after immersion in SBF solution for 2 h (*vide supra*, section 3.1.2). On increase in the immersion time up to 168 h, the agglomerates form a passive layer, which is formed due to deposition of hydroxides as manifest from corresponding enhanced EDX profile of oxygen atom. With the prolongation of immersion time, the whole surface was covered by nano-rods and large clusters were deposited over the samples. This is also evident from Fig. 6 (c) that the formation of $Zn(OH)_2$ nano-strands or agglomerates observed compared to nano-fibers in 6 (b) and polished zinc specimen 6 (a). This variation of morphology in zinc hydroxide (nano-fibers, agglomerates and nano-strand) is widely changed with varying concentrations of zinc ions [74]. The present finding of $Zn(OH)_2$ passive film formation after 2 h is corroborated with the results of section 3.1.2 (*vide supra*) and further evidence was given in subsequent XPS section (*vide infra*).

According to the EDX line scan profile, it can be seen that the corrosion product layer contains Zn, C, S and O, which were formed (zinc oxide/hydroxide/zinc carbonate) during the 168 h immersion time (Fig. 6 d). It was found that the intensity of the Zn signal from the corrosion layer became weaker than that of the substrate, since Zn dissolved during immersion and formed corrosion products at the interface.

An EDX analysis shows that Zn degradation is gradually increased in SBF. Meanwhile, zinc hydroxide remains the longer signal with constant immersion on the surface of the sample. Elemental mapping and the atomic percentage (see ESI† Figs. S1–S3 and Table S2) for the corresponding elements are also supporting the findings.

3.4.2. *XRD analysis*

The XRD pattern of Zn specimens in the presence and absence of SBF solution at 2 h and 168 h are shown in Fig. 7. The diffraction peak at about $2\theta = 36.27$ can be indexed to (002) is attributed to ZnO (zincite, JCPDS 36–1451), along with other main peaks at 39.13 , 54.35 can be indexed to (311) (110) corresponding to the $Zn(OH)_2$ orthorhombic structure (wulfingite, JCPDS 38–0385). Additionally, secondary peaks at 69.93 and 77.16 corresponding to (112) (202) also confirm $Zn(OH)_2$ [75]. Moreover, the intensities of the dominant peaks are strengthened on all XRD profile in 168 h of exposure period promotes the formation of $Zn(OH)_2$ confirming the predictions of higher exposure period favored for the transformation from ZnO. Low intensity significant peaks (inset of Fig. 7) at 28.08 (102, JCPDS 09–0432), 30.75 (241, JCPDS 74–2275), and 32.76 (104, JCPDS 8–0049) were observed with the time prolonged, indicating the formation of Ca_3 $(PO_4)_2$, $Zn_3(PO_4)_2$, and $ZnCO_3$ respectively on surface is apparent after immersion for longer time [53] (see ESI† and Table S3). The absence of peaks from corrosion products comprises the amorphous state of corrosion products in 2 h of immersion.

3.4.3. *XPS analysis*

Fig. 8 shows the XPS analysis of Zn alloy samples immersed in the SBF solution after 2 h and 168 h, which is used to assess the chemical composition of the samples. The C 1s spectra for 2 h and 168 h (Fig. 8 (b-c)) indicates the presence of C on the Zn-alloy surface. The 2 h sample indicates the presence of adventitious carbon (binding energy 284.8 eV) [76], whereas the 168 h sample indicates the presence of adventitious carbon along with a higher amount of carbonate carbon (binding energy 287.5 eV) [77]. The small binding peak at 291.7 eV can be clearly observed, providing evidence of trapped CO_2 in the corrosion product [78]. The formation of the Zn–OH on the specimen surface has been confirmed from the peak at 531.4 eV corresponding to the O 1s spectra ((Fig. 8 (d)) [75](along with this some oxoanions like, PO_4^{3-}, HPO_4^{2-} and CO_3^{2-} present in corrosion products in prolonged exposure period. Fig. 8 (e). spectra display a maxima in the range of 533

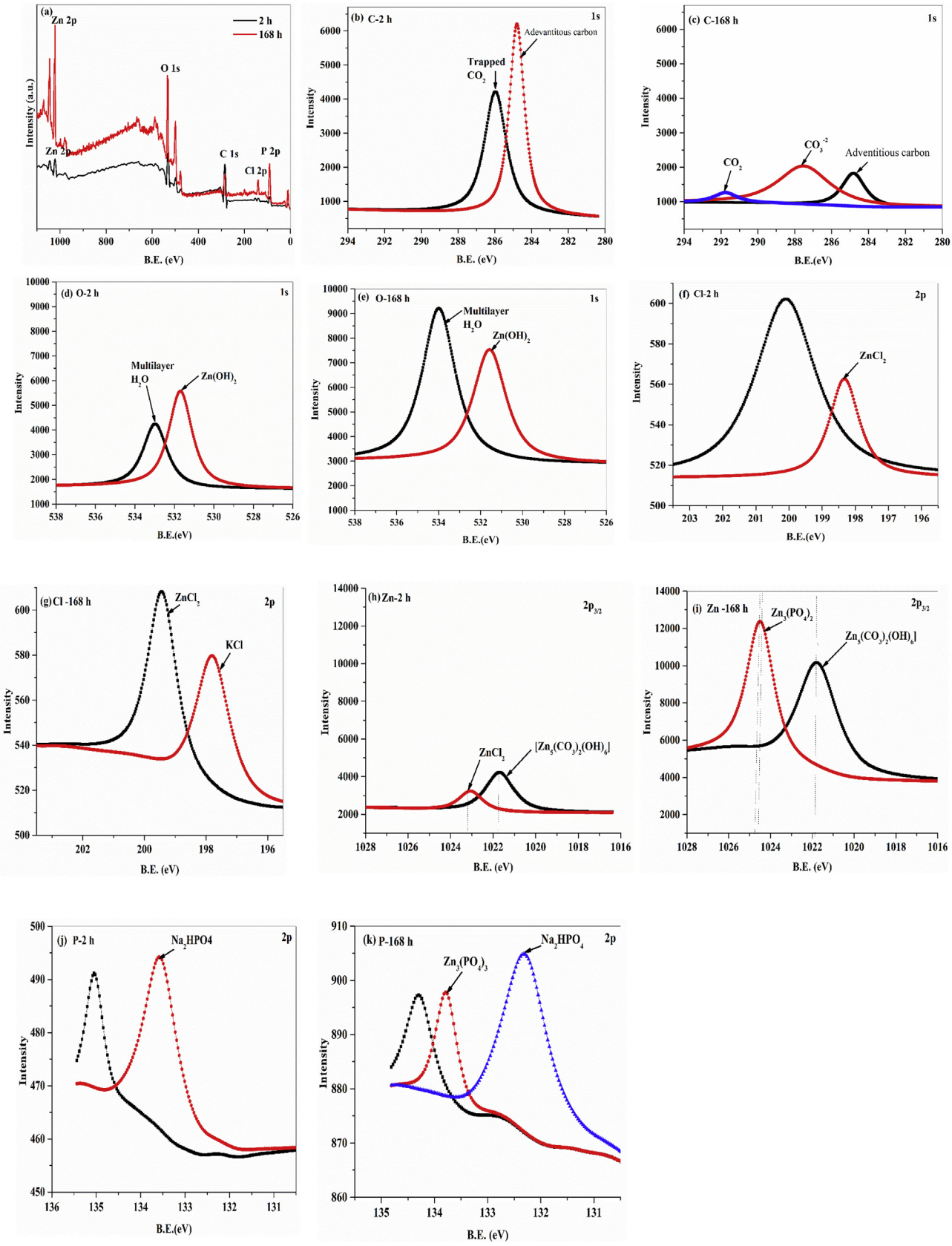

Fig. 8 – XPS spectra of Zn alloy (a) XPS survey overview spectra (b–c) after immersion of C 1s for 2 h and 168 h in SBF (d–e) after immersion of O 1s for 2 h and 168 h in SBF (f–g) after immersion of Zn 2p for 2 h and 168 h in SBF (h–i) after immersion of Cl 2p for 2 h and 168 h (j, k) after immersion of P 2p for 2 h and 168 h in SBF.

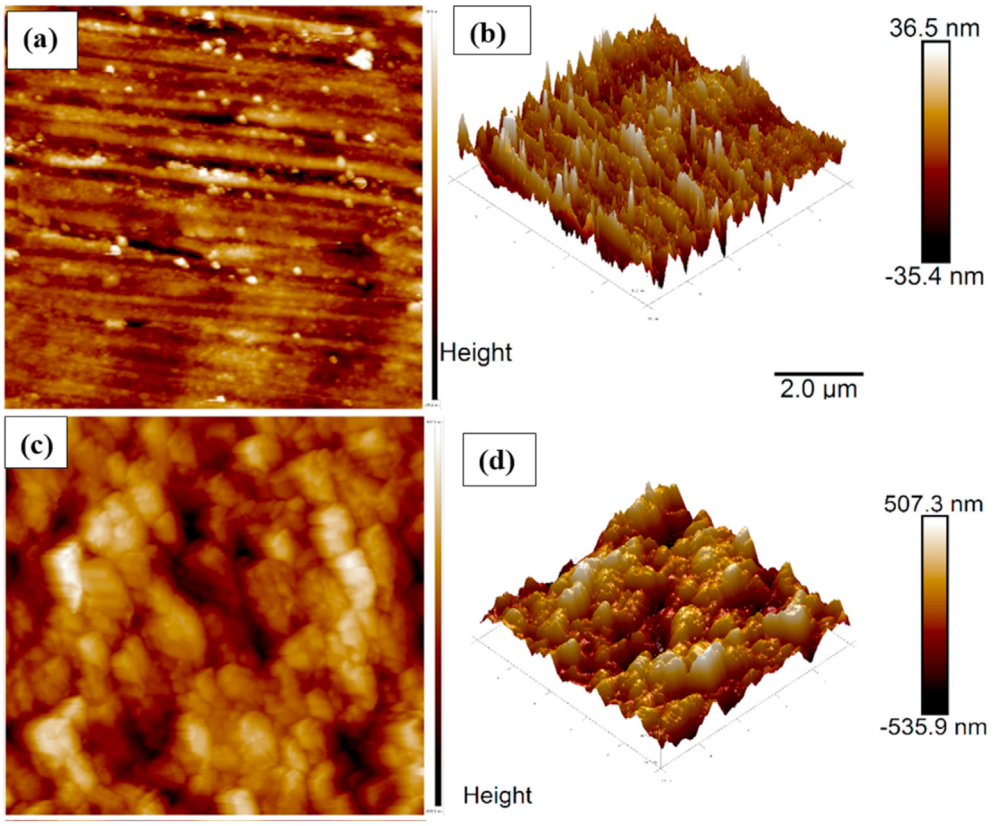

Fig. 9 – 2-D and 3-D atomic microscope image of Zn alloy in SBF solution (a–b) polished Zn alloy (c–d) 168 h immersion period.

and 534 eV confirmed the adsorbed multilayer H_2O on zinc specimen corrosion product [79,80]. The presence of Cl on the surface of the Zn alloy as part of the corrosion product was also established by XPS analysis (Fig. 8 (f, g)). The 198.3 eV and 199.5 eV binding energy is assigned for Cl 2p signal for $ZnCl_2$ species (2 h and 168 h sample) [81] and 197.8 eV binding energy corresponds to presence of Cl as part of KCl [82]. The binding energy of 1021.6 eV is associated with Zn $2p_{3/2+}$electron. This band aging suggests that the Zn present as basic zinc carbonate or probably as hydrozincite [$Zn_5(CO_3)_2(OH)_6$], in both 2 h and 168 h samples (Fig. 8 (h, i)) [65]. A small peak at 1023.1 eV in the 2 h sample indicates the presence of Zn as $ZnCl_2$ which is not present in the 168 h sample. The disappearance of 1023.1 eV binding energy peak in the 168 h sample indicates the transformation of $ZnCl_2$ as a different corrosion product [83]. A binding energy peak at 1024.5 eV in the 168 h sample indicates the presence of Zn as $Zn_3(PO_4)_2$. The further analysis of Fig. 8 (j) and (k) indicates the accumulation of $Zn_3(PO_4)_2$ as a corrosion product. The peaks P, 2p shifted towards lower binding energy in the P and P + Zn absorption system, also exhibits a similar chemical environment for phosphorus [84]. The ratio 1:2 of Zn/Cl was observed, which confirmed the formation of $ZnCl_2$. However, The range of 1:1 and 3:2 was observed for Zn/O, Zn/P further confirmation of $Zn(OH)_2$, $Zn_3(PO_4)_2$ compound on the surface of Zn alloy.

3.4.4. *Atomic force microscopy (AFM)*

The changes in topography on the Zn alloy surface were examined with AFM technique (2-D and 3-D tapping mode). The surface topography of the Zn alloy changes with increase in immersion time. The polished surface of the Zn alloy, revealed a flat substrate, consisting of small nodular structures, which, apparently, are ordered along the polishing lines (Fig. 9 a, b). The average roughness (Ra) of the metal alloy were 6.87 nm. After increasing the immersion time to 168 h, the substrate surface looks rougher and the grain was observed with an average roughness (R_a) of 115 nm (Fig. 9 c, d).

4. Conclusion

The initial corrosion behavior of Zn alloy in SBF solution was investigated by immersion, electrochemical and surface analysis up to 168 h to estimate the longevity of these implantation materials. The Zn alloy displayed a uniform corrosion rate in SBF solution via an immersion test. A homogenous distribution of corrosion products occurs on the metal alloy surface. After 120 h of immersion time, the stable corrosion products were formed over the surface of the Zn alloy, which caused a passivation on the surface of Zn alloy. The initial corrosion products mainly ZnO, $Zn(OH)_2$ [$Zn_5(CO_3)_2(OH)_6$], $Zn_3(PO_4)_2$, $ZnCl_2$, etc. were obtained during the immersion time, which was confirmed by XPS, SEM analysis. From the XPS analysis, binding energy shifts in Zn $2p_{3/2}$ combined with P 2p and Cl 2p spectra agrees with Zn $2p_{3/2}$ spectra, confirming the formation of $Zn_3(PO_4)_2$, $ZnCl_2$ respectively. Surface roughness and morphology was increased with exposure time in SBF solution and crystalline nature of the Zn

alloy was evaluated by XRD analysis. Hence, these observations support the uses of Zn alloy in orthopedic implantation as a biodegradable material.

Note

XPS values obtained from NIST database (NIST XPS database version 4.1).

Declaration of Competing Interest

The authors declare that they have no known competing financial interests or personal relationships that could have appeared to influence the work reported in this paper.

Appendix A. Supplementary data

Supplementary data to this article can be found online at https://doi.org/10.1016/j.jmrt.2020.12.050.

REFERENCES

[1] Zhao S, Seitz JM, Eifler R, Maier HJ, Guillory RJ, Earley EJ, et al. Zn-Li alloy after extrusion and drawing: structural, mechanical characterization, and biodegradation in abdominal aorta of rat. Mater Sci Eng C 2017;76:301–12. https://doi.org/10.1016/j.msec.2017.02.167.

[2] Zhao H, Humbeeck J Van, Sohier J, De Scheerder I. Electrochemical polishing of 316L stainless steel slotted tube coronary stents. J Mater Sci Mater Med 2002;13:911–6. https://doi.org/10.1023/A:1019831808503.

[3] Liu X, Chu PK, Ding C. Surface modification of titanium, titanium alloys, and related materials for biomedical applications. Mater Sci Eng R Rep 2004;47:49–121. https://doi.org/10.1016/j.mser.2004.11.001.

[4] Li Y, Munir KS, Lin J, Wen C. Titanium-niobium pentoxide composites for biomedical applications. Bioact Mater 2016;1:127–31. https://doi.org/10.1016/j.bioactmat.2016.10.001.

[5] Bao Y, Krishnan KM. Preparation of functionalized and gold-coated cobalt nanocrystals for biomedicalapplications. J Magn Magn Mater 2005;293:15–9. https://doi.org/10.1016/j.jmmm.2005.01.037.

[6] Disegi JA, Kennedy RL, Pilliar R. Cobalt-base alloys for biomedical applications. 1999. https://doi.org/10.1520/stp1365-eb.

[7] Ghoneim AA, El-Kamel RS, Fekry AM. Hydrogen evolution and quantum calculations for potassium sorbate as an efficient green inhibitor for biodegradable magnesium alloy staples used for sleeve gastrectomy surgery. Int J Hydrogen Energy 2020;45:24370–82. https://doi.org/10.1016/j.ijhydene.2020.06.260.

[8] El-Kamel RS, Ghoneim AA, Fekry AM. Electrochemical, biodegradation and cytotoxicity of graphene oxide nanoparticles/polythreonine as a novel nano-coating on AZ91E Mg alloy staple in gastrectomy surgery. Mater Sci Eng C 2019;103:109780. https://doi.org/10.1016/j.msec.2019.109780.

[9] Fekry AM. Electrochemical behavior of a novel nano-composite coat on Ti alloy in phosphate buffer solution for biomedical applications. RSC Adv 2016;6:20276–85. https://doi.org/10.1039/c6ra01064d.

[10] Fekry AM, Ahmed RA, Bioumy SA. Silver nanoparticle/graphene oxide/chitosan coatings for protection of surfaces in food processing. J Bio- Tribo-Corrosion 2020;6:1–16. https://doi.org/10.1007/s40735-020-00402-6.

[11] Farghali RA, Fekry AM, Ahmed RA, Elhakim HKA. Corrosion resistance of Ti modified by chitosan-gold nanoparticles for orthopedic implantation. Int J Biol Macromol 2015;79:787–99. https://doi.org/10.1016/j.ijbiomac.2015.04.078.

[12] Ameer MA, Ghoneim AA, Fekry AM. Electrochemical and interface analysis of titanium alloy in simulated body fluid. Surf Interface Anal 2014;46:65–71. https://doi.org/10.1002/sia.5349.

[13] Ahmed RA, Fekry AM, Farghali RA. A study of calcium carbonate/multiwalled-carbon nanotubes/chitosan composite coatings on Ti-6Al-4V alloy for orthopedic implants. Appl Surf Sci 2013;285:309–16. https://doi.org/10.1016/j.apsusc.2013.08.056.

[14] Purnama A, Hermawan H, Mantovani D. Biodegradable metal stents: a focused review on materials and clinical studies. J Biomater Tissue Eng 2014;4:868–74. https://doi.org/10.1166/jbt.2014.1263.

[15] Li H, Zheng Y, Qin L. Progress of biodegradable metals. Prog Nat Sci Mater Int 2014;24:414–22. https://doi.org/10.1016/j.pnsc.2014.08.014.

[16] Bowen PK, Drelich J, Goldman J. Zinc exhibits ideal physiological corrosion behavior for bioabsorbable stents. Adv Mater 2013;25:2577–82. https://doi.org/10.1002/adma.201300226.

[17] Murni NS, Dambatta MS, Yeap SK, Froemming GRA, Hermawan H. Cytotoxicity evaluation of biodegradable Zn-3Mg alloy toward normal human osteoblast cells. Mater Sci Eng C 2015;49:560–6. https://doi.org/10.1016/j.msec.2015.01.056.

[18] Chandra RK. Excessive intake of zinc impairs immune responses. JAMA, J Am Med Assoc 1984;252:1443–6. https://doi.org/10.1001/jama.1984.03350110043027.

[19] Vallee BL, Falchuk KH. Zinc and gene expression. Philos Trans R Soc Lond B Biol Sci 1981;294:185–97. https://doi.org/10.1098/rstb.1981.0098.

[20] MacDonald Ruth S. The role of zinc in growth and cell proliferation. J Nutr 2000 May;130(5):1500S–8S. https://doi.org/10.1093/jn/130.5.1500S.

[21] Lansdown ABG, Mirastschijski U, Stubbs N, Scanlon E, Ågren MS. Zinc in wound healing: theoretical, experimental, and clinical aspects. Wound Repair Regen 2007;15:2–16. https://doi.org/10.1111/j.1524-475X.2006.00179.x.

[22] Alscher DM, Biegger D, Kuhlmann U, Fritz P. Induction of metallothionein in mesothelial cells by zinc. Artif Organs 2007;31:488–91. https://doi.org/10.1111/j.1525-1594.2007.00412.x.

[23] Vallee BL, Auld DS. Zinc coordination, function, and structure of zinc enzymes and other proteins. Biochemistry 1990;29:5647–59. https://doi.org/10.1021/bi00476a001.

[24] Nelbach ME, Pigiet VP, Gerhart JC, Schachman HK. Escherichia coli. Biochemistry 1970;11:315–27.

[25] Bonam D, Ludden PW. Purification and characterization of carbon monoxide dehydrogenase, a nickel, zinc, iron-sulfur protein, from Rhodospirillum rubrum. J Biol Chem 1987;262:2980–7.

[26] Morita Y, Sawada M, Seno H, Takaishi S, Fukuzawa H, Miyake N, et al. Identification of xanthine dehydrogenase/xanthine oxidase as a rat Paneth cell zinc-binding protein. Biochim Biophys Acta Mol Cell Res 2001;1540:43–9. https://doi.org/10.1016/S0167-4889(01)00118-5.

[27] Plum LM, Rink L, Hajo H. The essential toxin: impact of zinc on human health. Int J Environ Res Publ Health 2010;7:1342–65. https://doi.org/10.3390/ijerph7041342.
[28] Choi J, Kim H, Kim P, Jo E, Kim HM, Lee MY, et al. Toxicity of zinc oxide nanoparticles in rats treated by two different routes: single intravenous injection and single oral administration. J Toxicol Environ Health Part A Curr Issues 2015;78:226–43. https://doi.org/10.1080/15287394.2014.949949.
[29] Eggleton WGE. The zinc and copper contents of the organs and tissues of Chinese subjects. Biochem J 2015;34:991–7. https://doi.org/10.1042/bj0340991.
[30] Li HF, Xie XH, Zheng YF, Cong Y, Zhou FY, Qiu KJ, et al. Development of biodegradable Zn-1X binary alloys with nutrient alloying elements Mg, Ca and Sr. Sci Rep 2015;5:1–14. https://doi.org/10.1038/srep10719.
[31] Crichton RR. Zinc: lewis acid and gene regulator. Biol Inorg Chem 2008:197–210. https://doi.org/10.1016/b978-044452740-0.50012-0.
[32] Guillory RJ, Bowen PK, Hopkins SP, Shearier ER, Earley EJ, Gillette AA, et al. Corrosion characteristics dictate the long-term inflammatory profile of degradable zinc arterial implants. ACS Biomater Sci Eng 2016;2:2355–64. https://doi.org/10.1021/acsbiomaterials.6b00591.
[33] Liu X, Sun J, Zhou F, Yang Y, Chang R, Qiu K, et al. Micro-alloying with Mn in Zn-Mg alloy for future biodegradable metals application. Mater Des 2016;94:95–104. https://doi.org/10.1016/j.matdes.2015.12.128.
[34] Zhang S, Zhang X, Zhao C, Li J, Song Y, Xie C, et al. Research on an Mg-Zn alloy as a degradable biomaterial. Acta Biomater 2010;6:626–40. https://doi.org/10.1016/j.actbio.2009.06.028.
[35] Tang Z, Niu J, Huang H, Zhang H, Pei J, Ou J, et al. Potential biodegradable Zn-Cu binary alloys developed for cardiovascular implant applications. J Mech Behav Biomed Mater 2017;72:182–91. https://doi.org/10.1016/j.jmbbm.2017.05.013.
[36] Niu J, Tang Z, Huang H, Pei J, Zhang H, Yuan G, et al. Research on a Zn-Cu alloy as a biodegradable material for potential vascular stents application. Mater Sci Eng C 2016;69:407–13. https://doi.org/10.1016/j.msec.2016.06.082.
[37] Tang Z, Huang H, Niu J, Zhang L, Zhang H, Pei J, et al. Design and characterizations of novel biodegradable Zn-Cu-Mg alloys for potential biodegradable implants. Mater Des 2017;117:84–94. https://doi.org/10.1016/j.matdes.2016.12.075.
[38] Lin W, Yang H, Wang C, Liu C, Chen H, Wu Y. Evolution of the degradation mechanism of pure zinc stent in the one-year study of rabbit abdominal aorta model Biomaterials Evolution of the degradation mechanism of pure zinc stent in the one- year study of rabbit abdominal aorta model. Biomaterials 2017;145:92–105. https://doi.org/10.1016/j.biomaterials.2017.08.022.
[39] Törne K, Larsson M, Norlin A, Weissenrieder J. Degradation of zinc in saline solutions, plasma, and whole blood. J Biomed Mater Res B Appl Biomater 2016;104:1141–51. https://doi.org/10.1002/jbm.b.33458.
[40] Ma J, Zhao N, Zhu D. Endothelial cellular responses to biodegradable metal zinc. ACS Biomater Sci Eng 2015;1:1174–82. https://doi.org/10.1021/acsbiomaterials.5b00319.
[41] Ma J, Zhao N, Zhu D. Bioabsorbable zinc ion induced biphasic cellular responses in vascular smooth muscle cells. Nat Publ Gr 2016:1–10. https://doi.org/10.1038/srep26661.
[42] Zhu D, Su Y, Young ML, Ma J, Zheng Y, Tang L. Biological responses and mechanisms of human bone marrow mesenchymal stem cells to Zn and Mg biomaterials. ACS Appl Mater Interfaces 2017;9:27453–61. https://doi.org/10.1021/acsami.7b06654.
[43] Shearier ER, Bowen PK, He W, Drelich A, Drelich J, Goldman J, et al. In vitro cytotoxicity, adhesion, and proliferation of human vascular cells exposed to zinc. ACS Biomater Sci Eng 2016;2:634–42. https://doi.org/10.1021/acsbiomaterials.6b00035.
[44] Wang B, Xu D, Dong J, Ke W. Effect of texture on biodegradable behavior of an as-extruded Mg-3 % Al- 1 % Zn alloy in phosphate buffer saline medium journal of materials science & technology effect of texture on biodegradable behavior of an as-extruded Mg – 3 % Al – 1 % Zn alloy in P. J Mater Sci Technol 2016;32:646–52. https://doi.org/10.1016/j.jmst.2016.02.002.
[45] Yamamoto A, Hiromoto S. Effect of inorganic salts , amino acids and proteins on the degradation of pure magnesium in vitro. Mater Sci Eng C 2009;29:1559–68. https://doi.org/10.1016/j.msec.2008.12.015.
[46] Jamesh MI, Wu G, Zhao Y, Mckenzie DR, Bilek MMM, Chu PK. Electrochemical corrosion behavior of biodegradable Mg – Y – RE and Mg- Zn-Zr alloys in ringer ' s solution and simulated body fluid. Corrosion Sci 2014. https://doi.org/10.1016/j.corsci.2014.11.015.
[47] Kokubo T, Takadama H. How useful is SBF in predicting in vivo bone bioactivity? Biomaterials 2006;27:2907–15. https://doi.org/10.1016/j.biomaterials.2006.01.017.
[48] Miklaszewski A, Jurczyk MU, Jurczyk M. Microstructural development of Ti e B alloyed layer for hard tissue applications. J Mater Sci Technol 2013;29:565–72. https://doi.org/10.1016/j.jmst.2013.02.014.
[49] Wang C, Yu Z, Cui Y, Zhang Y, Yu S, Qu G, et al. Processing of a novel Zn alloy micro-tube for biodegradable vascular stent application. J Mater Sci Technol 2016. https://doi.org/10.1016/j.jmst.2016.08.008.
[50] Ishida N, Abidin Z, Martin D, Atrens A. Corrosion of high purity Mg , AZ91 , ZE41 and Mg2Zn0 . 2Mn in Hank ' s solution at room temperature. Corrosion Sci 2011;53:862–72. https://doi.org/10.1016/j.corsci.2010.10.008.
[51] Müller L, Müller FA. Preparation of SBF with different HCO3- content and its influence on the composition of biomimetic apatites. Acta Biomater 2006;2:181–9. https://doi.org/10.1016/j.actbio.2005.11.001.
[52] Vojtěch D, Kubásek J, Šerák J, Novák P. Mechanical and corrosion properties of newly developed biodegradable Zn-based alloys for bone fixation. Acta Biomater 2011;7:3515–22. https://doi.org/10.1016/j.actbio.2011.05.008.
[53] Liu L, Meng Y, Dong C, Yan Y, Volinsky AA, Wang LN. Initial formation of corrosion products on pure zinc in simulated body fluid. J Mater Sci Technol 2018;34:2271–82. https://doi.org/10.1016/j.jmst.2018.05.005.
[54] Diggle JW, Downie TC, Goulding CW. A study of the formation and dissolution of porous anodic oxide films on aluminum: behavior of the porous layer. J Electrochem Soc 2007;116:1347. https://doi.org/10.1149/1.2411516.
[55] Hunter MS, Fowle P. Natural and thermally formed oxide films on aluminum. J Electrochem Soc 2007;103:482. https://doi.org/10.1149/1.2430389.
[56] Vrublevsky I, Parkoun V, Schreckenbach J. Analysis of porous oxide film growth on aluminum in phosphoric acid using re-anodizing technique. Appl Surf Sci 2005;242:333–8. https://doi.org/10.1016/j.apsusc.2004.08.034.
[57] Moon SM, Pyun S Il. Growth mechanism of anodic oxide films on pure aluminium in aqueous acidic and alkaline solutions. J Solid State Electrochem 1998;2:156–61. https://doi.org/10.1007/s100080050081.
[58] Jagminas A, Vrublevsky I, Kuzmarskyte J, Jasulaitiene V. Composition, structure and electrical properties of alumina barrier layers grown in fluoride-containing oxalic acid solutions. Acta Mater 2008;56:1390–8. https://doi.org/10.1016/j.actamat.2007.11.029.

[59] Abd El Haleem SM, Abd El Wanees S, Abd El Aal EE, Farouk A. Factors affecting the corrosion behaviour of aluminium in acid solutions . I . Nitrogen and/or sulphur-containing organic compounds as corrosion inhibitors for Al in HCl solutions. Corrosion Sci 2013;68:1–13. https://doi.org/10.1016/j.corsci.2012.03.021.

[60] Abdel Rehim SS, Hassan HH, Amin MA. Galvanostatic anodization of pure Al in some aqueous acid solutions. Part I: growth kinetics, composition and morphological structure of porous and barrier-type anodic alumina films. J Appl Electrochem 2002;32:1257–64. https://doi.org/10.1023/A:1021662814303.

[61] Abd El Haleem SM, Abd El Wanees S, Abd El Aal EE, Diab A. Environmental factors affecting the corrosion behavior of reinforcing steel II . Role of some anions in the initiation and inhibition of pitting corrosion of steel in Ca (OH) 2 solutions. Corrosion Sci 2010;52:292–302. https://doi.org/10.1016/j.corsci.2009.09.004.

[62] Jo JH, Kang BG, Shin KS, Kim HE, Hahn BD, Park DS, et al. Hydroxyapatite coating on magnesium with MgF2 interlayer for enhanced corrosion resistance and biocompatibility. J Mater Sci Mater Med 2011;22:2437–47. https://doi.org/10.1007/s10856-011-4431-3.

[63] Escudero ML, Ruano OA, Garcia-Alonso MC, del Valle JA, Fernandez-Lorenzo M, Alvarez-Lopez M, et al. Corrosion behaviour of AZ31 magnesium alloy with different grain sizes in simulated biological fluids. Acta Biomater 2009;6:1763–71. https://doi.org/10.1016/j.actbio.2009.04.041.

[64] Baril G, Blanc C, Pébère N. AC impedance spectroscopy in characterizing time-dependent corrosion of AZ91 and AM50 magnesium alloys characterization with respect to their microstructures. J Electrochem Soc 2002;148:B489. https://doi.org/10.1149/1.1415722.

[65] Hsu CH, Mansfeld F. Concernng the conversion of the constant phase element parameter Y0into a capacitance. Corrosion 2001;57:747–8. https://doi.org/10.5006/1.3280607.

[66] Brug GJ, van den Eeden ALG, Sluyters-Rehbach M, Sluyters JH. The analysis of electrode impedances complicated by the presence of a constant phase element. J Electroanal Chem Interfacial Electrochem 1984;176:275–95.

[67] Geary SAAL, Metals. Electrochemical polarization. J Electrochem Soc 1957;104:56–63. https://doi.org/10.1149/1.2428496.

[68] Yadav AP, Nishikata A, Tsuru T. Oxygen reduction mechanism on corroded zinc. J Electroanal Chem 2005;585:142–9. https://doi.org/10.1016/j.jelechem.2005.08.007.

[69] Yang J, Yim CD, You BS. Effects of solute Zn on corrosion film of Mg–Sn–Zn alloy formed in NaCl solution. J Electrochem Soc 2016;163:C839–44. https://doi.org/10.1149/2.0401614jes.

[70] Despić A, Parkhutik VP. Electrochemistry of aluminum in aqueous solutions and physics of its anodic oxide. Mod Aspect Electrochem 2013:401–503. https://doi.org/10.1007/978-1-4684-8762-6_6.

[71] Ambat R, Aung NN, Zhou W. Effect of pH and chloride ion concentration on inhibitor storage in amorphous Al-Co-Ce alloys. Smart Coatings Adv Funct With New Mater 2010:785–93. https://doi.org/10.1142/9789812811431_0093.

[72] Gudić S, Radošević J, Višekruna A, Kliškić M. Oxide film growth on Al-In alloys in a borate buffer solution in conditions of galvanostatic anodising. Electrochim Acta 2004;49:773–83. https://doi.org/10.1016/j.electacta.2003.09.031.

[73] Mazhar AA, Badawy WA, Abou-Romia MM. Impedance studies of corrosion resistance of aluminium in chloride media. Surf Coating Technol 1986;29:335–45. https://doi.org/10.1016/0257-8972(86)90006-X.

[74] Peng X, Jin J, Kobayashi N, Schmitt W, Ichinose I. Time-dependent growth of zinc hydroxide nanostrands and their crystal structure. Chem Commun 2008;16:1904–6. https://doi.org/10.1039/b719497h.

[75] Oliva-avil AI. Investigation of the selective growth of ZnO and Zn (OH) 2 films deposited by chemical bath near room temperature. ECS J Solid State Sci Technol 2017;6:N45–53. https://doi.org/10.1149/2.0051707jss.

[76] Aswal DK, Muthe KP, Tawde S, Chodhury S, Bagkar N, Singh A, et al. XPS and AFM investigations of annealing induced surface modifications of MgO single crystals. J Cryst Growth 2002;236:661–6. https://doi.org/10.1016/S0022-0248(02)00852-7.

[77] Morettit G, Fierro G, Lo Jacono M, Porta P. Characterization of CuO-ZnO catalysts by X-ray photoelectron Spectroscopy: precursors , calcined and reduced samples*. Surf Interface Anal 1989;14:325–36.

[78] Manne R. Molecular spectroscopy by means of ESCA III . Carbon compounds molecular spectroscopy by means of ESCA III. Carbon compounds. Phys Scripta 1970;2:70–80. https://doi.org/10.1088/0031-8949/2/1-2/014.

[79] Wagner CD, Gale LH, Raymond RH, Kor A, La A. Two-dimensional chemical state Plots: a standardized data set for use in identifying chemical states by X-ray photoelectron spectroscopy. Anal Chem 1979;51:1979.

[80] Casalongue HS, Kaya S, Viswanathan V, Miller DJ, Friebel D, Hansen HA, et al. Direct observation of the oxygenated species during oxygen reduction on a platinum fuel cell cathode. Nat Commun 2013;4:2817. https://doi.org/10.1038/ncomms3817.

[81] Klein JC, Hercules DM. Surface characterization of model Urushibara catalysts. J Catal 1983;82:424–41. https://doi.org/10.1016/0021-9517(83)90209-9.

[82] Wren AG, Phillips RW, Tolentino LU. Surface reactions of chlorine molecules and atoms with water and sulfuric acid at low temperatures. J Colloid Interface Sci 1979;70:544–57. https://doi.org/10.1016/0021-9797(79)90062-6.

[83] Seals RD, Alexander R, Taylor LT, Dillard JG. Core electron binding energy study of group IIb-VIIa compounds. Inorg Chem 1973;12:2485–7.

[84] Liu J, Zhu R, Xu T, Xu Y, Ge F, Xi Y, et al. Co-adsorption of phosphate and zinc(II) on the surface of ferrihydrite. Chemosphere 2016;144:1148–55. https://doi.org/10.1016/j.chemosphere.2015.09.083.